A&A 627, A49 (2019)
https://doi.org/10.1051/0004-6361/201935460

Astronomy & Astrophysics

The CARMENES search for exoplanets around M dwarfs

Two temperate Earth-mass planet candidates around Teegarden's Star*

M. Zechmeister[1], S. Dreizler[1], I. Ribas[2,3], A. Reiners[1], J. A. Caballero[4], F. F. Bauer[5], V. J. S. Béjar[6,7], L. González-Cuesta[6,7], E. Herrero[2,3], S. Lalitha[1], M. J. López-González[5], R. Luque[6,7], J. C. Morales[2,3], E. Pallé[6,7], E. Rodríguez[5], C. Rodríguez López[5], L. Tal-Or[8,1], G. Anglada-Escudé[9,5], A. Quirrenbach[10], P. J. Amado[5], M. Abril[5], F. J. Aceituno[5], J. Aceituno[11,5], F. J. Alonso-Floriano[12], M. Ammler-von Eiff[13,18], R. Antona Jiménez[5], H. Anwand-Heerwart[1], B. Arroyo-Torres[11], M. Azzaro[11], D. Baroch[2,3], D. Barrado[4], S. Becerril[5], D. Benítez[11], Z. M. Berdiñas[14], G. Bergond[11], P. Bluhm[10], M. Brinkmöller[10], C. del Burgo[15], R. Calvo Ortega[5], J. Cano[16], C. Cardona Guillén[6,7], J. Carro[16], M. C. Cárdenas Vázquez[17], E. Casal[5], N. Casasayas-Barris[6,7], V. Casanova[5], P. Chaturvedi[18], C. Cifuentes[4,16], A. Claret[5], J. Colomé[2,3], M. Cortés-Contreras[4], S. Czesla[19], E. Díez-Alonso[16,20], R. Dorda[16,6,7], M. Fernández[5], A. Fernández-Martín[11], B. Fuhrmeister[19], A. Fukui[6,21], D. Galadí-Enríquez[11], I. Gallardo Cava[22,16], J. Garcia de la Fuente[11], A. Garcia-Piquer[2,3], M. L. García Vargas[23], L. Gesa[2,3], J. Góngora Rueda[11], E. González-Álvarez[24], J. I. González Hernández[6,7], R. González-Peinado[16], U. Grözinger[17], J. Guàrdia[2,3], A. Guijarro[11], E. de Guindos[11], A. P. Hatzes[18], P. H. Hauschildt[19], R. P. Hedrosa[11], J. Helmling[11], T. Henning[17], I. Hermelo[11], R. Hernández Arabi[11], L. Hernández Castaño[11], F. Hernández Otero[11], D. Hintz[19], P. Huke[1], A. Huber[17], S. V. Jeffers[1], E. N. Johnson[1], E. de Juan[11], A. Kaminski[10], J. Kemmer[10], M. Kim[25,10], H. Klahr[17], R. Klein[17], J. Klüter[10], A. Klutsch[26,16], D. Kossakowski[17], M. Kürster[17], F. Labarga[16], M. Lafarga[2,3], M. Llamas[16], M. Lampón[5], L. M. Lara[5], R. Launhardt[17], F. J. Lázaro[16], N. Lodieu[6,7], M. López del Fresno[4], M. López-Puertas[5], J. F. López Salas[11], J. López-Santiago[27,28], H. Magán Madinabeitia[11,10], U. Mall[17], L. Mancini[29,17,30,31], H. Mandel[10], E. Marfil[16], J. A. Marín Molina[11], D. Maroto Fernández[11], E. L. Martín[24], P. Martín-Fernández[11], S. Martín-Ruiz[5], C. J. Marvin[1], E. Mirabet[5,2,3], P. Montañés-Rodríguez[6,7], D. Montes[16], M. E. Moreno-Raya[32,11], E. Nagel[19], V. Naranjo[17], N. Narita[6,33,34,35,36], L. Nortmann[6,7], G. Nowak[6,7], A. Ofir[37], M. Oshagh[1], J. Panduro[17], H. Parviainen[6,7], J. Pascual[5], V. M. Passegger[19], A. Pavlov[17], S. Pedraz[11], A. Pérez-Calpena[23], D. Pérez Medialdea[5], M. Perger[2,3], M. A. C. Perryman[38], O. Rabaza[5], A. Ramón Ballesta[5], R. Rebolo[6,7], P. Redondo[6,7], S. Reffert[10], S. Reinhardt[11], P. Rhode[1], H.-W. Rix[17], F. Rodler[39,2,3], A. Rodríguez Trinidad[5], A. Rosich[2,3], S. Sadegi[10,17], E. Sánchez-Blanco[40], M. A. Sánchez Carrasco[5], A. Sánchez-López[5], J. Sanz-Forcada[4], P. Sarkis[17], L. F. Sarmiento[1], S. Schäfer[1], J. H. M. M. Schmitt[19], P. Schöfer[1], A. Schweitzer[19], W. Seifert[10], D. Shulyak[13,1], E. Solano[4], A. Sota[5], O. Stahl[10], S. Stock[10], J. B. P. Strachan[9], T. Stuber[10], J. Stürmer[41,10], J. C. Suárez[42,5], H. M. Tabernero[24], M. Tala Pinto[10], T. Trifonov[17], G. Veredas[10], J. I. Vico Linares[11], F. Vilardell[2,3], K. Wagner[10,17], V. Wolthoff[10], W. Xu[43], F. Yan[1], and M. R. Zapatero Osorio[24]

(Affiliations can be found after the references)

Received 13 March 2019 / Accepted 14 May 2019

ABSTRACT

Context. Teegarden's Star is the brightest and one of the nearest ultra-cool dwarfs in the solar neighbourhood. For its late spectral type (M7.0 V), the star shows relatively little activity and is a prime target for near-infrared radial velocity surveys such as CARMENES.
Aims. As part of the CARMENES search for exoplanets around M dwarfs, we obtained more than 200 radial-velocity measurements of Teegarden's Star and analysed them for planetary signals.
Methods. We find periodic variability in the radial velocities of Teegarden's Star. We also studied photometric measurements to rule out stellar brightness variations mimicking planetary signals.
Results. We find evidence for two planet candidates, each with 1.1 $M_\oplus$ minimum mass, orbiting at periods of 4.91 and 11.4 d, respectively. No evidence for planetary transits could be found in archival and follow-up photometry. Small photometric variability is suggestive of slow rotation and old age.
Conclusions. The two planets are among the lowest-mass planets discovered so far, and they are the first Earth-mass planets around an ultra-cool dwarf for which the masses have been determined using radial velocities.

Key words. methods: data analysis – planetary systems – stars: late-type – stars: individual: Teegarden's Star

* Tables D.1 and D.2 are only available at the CDS via anonymous ftp to cdsarc.u-strasbg.fr (130.79.128.5) or via http://cdsarc.u-strasbg.fr/viz-bin/qcat?J/A+A/627/A49

1. Introduction

Since the first exoplanet discoveries in the mid-1990s, more than 800 exoplanets have been detected with the radial-velocity (RV) method, while thousands of them have been detected with dedicated transit searches. Despite this great success, only very few planets have been found so far around dwarf stars later than M4.5 V, although these very late stellar types are very numerous. We know[1] only two planet hosts with effective temperatures cooler than 3000 K, but these are remarkable. One of them is Proxima Centauri (M5.5 V), which is the closest star to the Sun and hosts an Earth-mass planet in its habitable zone (Anglada-Escudé et al. 2016). The other one is TRAPPIST-1 (2MUCD 12171; M8.0 V), which hosts seven transiting planets and is located at a distance of 12.0 ± 0.4 pc (Gillon et al. 2016, 2017).

The paucity of planet detections around very late-type stars is mainly an observational bias due to the faintness in the visible wavelength range and red colours of these stars. The CARMENES[2] project (Quirrenbach et al. 2018), as well as a number of other projects (e.g. SPIRou[3], Donati et al. 2018; IRD[4], Kotani et al. 2018; HPF[5], Mahadevan et al. 2014; NIRPS[6], Wildi et al. 2017), aim to address this bias. Here we report the discovery of two planet candidates orbiting Teegarden's Star. First, we introduce the host star in Sect. 2. The RV measurements and the intensive photometric monitoring are presented in Sect. 3, and they are analysed in Sects. 4 and 5. The results are discussed in Sect. 6.

2. Teegarden's Star

2.1. Basic stellar parameters

Teegarden's Star was discovered in this century by Teegarden et al. (2003). It is the 24th nearest star to the Sun[7] with a distance of 3.831 pc. The spectral type is M7.0 V (Alonso-Floriano et al. 2015), making it the brightest representative of this and later spectral classes with a J magnitude of 8.39 mag ($V = 15.08$ mag). Schweitzer et al. (2019) derived the effective temperature $T_{\rm eff}$, metallicity [Fe/H], and surface gravity $\log g$ from fitting PHOENIX synthetic spectra (Husser et al. 2013) to CARMENES spectra following the method of Passegger et al. (2018). They obtained the luminosity L with *Gaia* DR2 parallax and integrated broad-band photometry as described in Cifuentes et al. (in prep.). Schweitzer et al. (2019) then estimated the stellar radius R via Stefan-Boltzmann's law and finally a stellar mass M of 0.089 $M_\odot$ by using their own linear mass-radius relation. Table 1 summarises a number of basic parameters mostly compiled from our M-dwarf database Carmencita (Caballero et al. 2016). For comparison, we also provide the $T_{\rm eff}$ from Rojas-Ayala et al. (2012) and [Fe/H] from Dieterich et al. (2014), pointing to disagreement of stellar parameter determination at the very cool end.

[1] http://exoplanets.org, accessed on 2019-04-10.
[2] Calar Alto high-Resolution search for M dwarfs with Exoearths with Near-infrared and optical Échelle Spectrographs.
[3] SPectropolarimètre InfraROUge.
[4] InfraRed Doppler spectrograph.
[5] Habitable Zone Planet Finder.
[6] Near Infra-Red Planet Searcher.
[7] http://www.astro.gsu.edu/RECONS/TOP100.posted.htm

Table 1. Stellar parameters for Teegarden's Star.

Parameter	Value	Ref.
Discovery name	Teegarden's Star	Tee03
Alias name	GAT 1370	Gat09
Karmn [(a)]	J02530 + 168	Cab16
α	02 53 00.89	*Gaia*
δ	+16 52 52.6	*Gaia*
$\mu_\alpha \cos\delta$ (mas yr^{-1})	3429.53 ± 0.33	*Gaia*
μ_δ (mas yr^{-1})	−3806.16 ± 0.31	*Gaia*
l (deg) [(b)]	45.82636650288	*Gaia*
b (deg) [(b)]	+0.30111982472	*Gaia*
π (mas)	261.01 ± 0.27	*Gaia*
	259.6 ± 0.6	Wei16
	259.3 ± 0.9	Gat09
d (pc)	3.831 ± 0.004	*Gaia*
V (mag)	15.08 ± 0.12	Hen15
J (mag)	8.39 ± 0.03	2MASS
Sp. type	M7.0 V	Alo15
$T_{\rm eff}$ (K)	2904 ± 51	Sch19
	2637 ± 30	Roj12
L ($L_\odot$)	0.000 73 ± 0.000 01	Sch19
	0.000 73 ± 0.000 02	Die14
R ($R_\odot$)	0.107 ± 0.004	Sch19
	0.127 ± 0.004	Die14
M ($M_\odot$)	0.089 ± 0.009	Sch19
[Fe/H] (dex)	−0.19 ± 0.16	Sch19
	−0.55 ± 0.17	Roj12
U (km s^{-1})	−69.46 ± 0.31	Cor16
V (km s^{-1})	−71.17 ± 0.15	Cor16
W (km s^{-1})	−58.68 ± 0.25	Cor16
γ (km s^{-1})	+68.375	Rei18
$v \sin i$ (km s^{-1})	<2	Rei18
$\log L_{\rm H\alpha}/L_{\rm bol}$	−5.37	This work
$\log L_{\rm X}/L_{\rm bol}$	< − 4.23	Ste14, this work
Age [Gyr]	>8	This work

Notes. [(a)]Carmencita identifier. [(b)]Heliocentric ecliptic longitude and latitude.
References. 2MASS: Skrutskie et al. (2006); Alo15: Alonso-Floriano et al. (2015); Cab16: Caballero et al. (2016); Cor16: Cortés Contreras (2016); Die14: Dieterich et al. (2014); *Gaia*: Gaia Collaboration (2018); Gat09: Gatewood & Coban (2009); Hen15: Henden et al. (2015); Rei18: Reiners et al. (2018); Roj12: Rojas-Ayala et al. (2012); Sch19: Schweitzer et al. (2019); Ste14: Stelzer et al. (2014); Tee03: Teegarden et al. (2003); Wei16: Weinberger et al. (2016).

2.2. Activity, rotation period, and age estimates

During their lifetime, low-mass stars lose angular momentum, leading to slower rotation and lower magnetic activity at old ages (e.g. Barnes 2007; Irwin & Bouvier 2009). Two useful measures of magnetic activity are non-thermal emissions in Hα and in X-rays. Reiners et al. (2018) reported for Teegarden's Star a normalised Hα luminosity of $\log L_{\rm H\alpha}/L_{\rm bol} = -5.18$ based on one CARMENES spectrum. The average over all CARMENES spectra is $\log L_{\rm H\alpha}/L_{\rm bol} = -5.25$. This value can be compared to other ultra-cool dwarfs, for example those measured in Reiners & Basri (2010). Out of their sample of 24 stars of spectral types M7.0 V and M7.5 V, only one exhibits Hα emission as low as Teegarden's Star (LP 321-222: $\log L_{\rm H\alpha}/L_{\rm bol} < -5.27$). In Jeffers et al. (2018), it also belonged to the least active

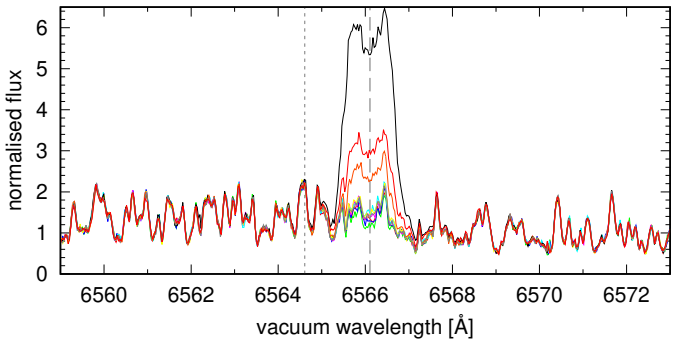

Fig. 1. Largest Hα flare (black) in our CARMENES data. These ten spectra were taken between 2017-10-26 and 2017-11-01. The vertical line marks Hα at rest wavelength ($\lambda_{\rm vac}$ = 6564.61 Å, grey dotted) and at a shift of γ = +68.375 km s^{-1} (grey dashed).

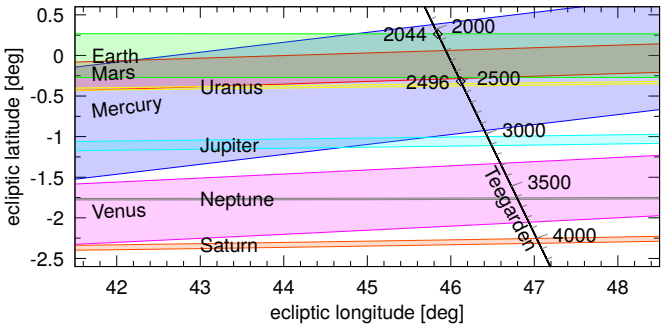

Fig. 2. Transits of solar system objects as seen from Teegarden's Star. Current location of transit regions for Earth (green), Mars (red), and Mercury (blue). The trace of Teegarden's Star (black) due to its proper motion is marked with first Earth transit (2044) and last Earth transit (2496).

stars in this spectral bin. However, Teegarden's Star exhibits occasional flares (Fig. 1), and $\log L_{\rm H\alpha}/L_{\rm bol}$ varies from −5.58 up to −4.26 during the CARMENES observations (see also Fig. 9).

The stellar rotation period of Teegarden's Star has not been measured. Newton et al. (2016) listed a photometric period of 18.460 d with an amplitude of 0.0013 ± 0.0021 mag based on MEarth data. Because the uncertainty is larger than the amplitude itself, a detection cannot be claimed. The line profiles of Teegarden's Star do not exhibit any significant rotational broadening in the CARMENES spectra ($v \sin i$ < 2 km s^{-1}, Reiners et al. 2018). When a stellar radius of 0.107 $R_\odot$ is assumed, this implies a minimum stellar rotation longer than $P_{\rm rot}$ > 2.7 d. To estimate the rotation period of Teegarden's Star, we can use Hα-$P_{\rm rot}$ relations. Newton et al. (2017) showed that stars with masses of about 0.1 $M_\odot$ and no significant Hα emission rotate at periods $P_{\rm rot} \approx$ 100 d or longer (see their Fig. 5). Similar estimates can be obtained from the works of West et al. (2015, Fig. 8) or Jeffers et al. (2018, Fig. 2).

The age of Teegarden's Star can be estimated in various ways. Again, the normalised Hα luminosity can be used. West et al. (2008) showed the distribution of Hα activity from an analysis of 38 000 M dwarfs. Their low-resolution Sloan Digital Sky Survey (SDSS) spectra are sensitive to Hα equivalent widths of 1 Å in emission, which translates into $\log L_{\rm H\alpha}/L_{\rm bol}$ well above −5 at this spectral type. From their data they concluded that stars of spectral type M7 V show emission in excess of this threshold for as long as $8.0^{+0.5}_{-1.0}$ Gyr. Our average measurements of Hα emission are significantly below this threshold, so that Teegarden's Star would be classified as inactive according to the work of West et al. (2008).

An X-ray measurement of Teegarden's Star was attempted by Stelzer et al. (2014), who reported an upper limit of $\log F_{\rm X}/{\rm mW\,m^2} < -13.03$ from the non-detection. Normalised with an updated bolometric flux of $\log F_{\rm bol}/{\rm mW\,m^2} < -8.79$ (calculated with distances and luminosity from Table 1), this upper limit of $\log L_{\rm X}/L_{\rm bol} < -4.23$ does not provide strong constraints on age or rotation rate, but it is consistent with our conclusions from the Hα measurement (see, e.g., Wright et al. 2011; Reiners et al. 2014).

The age has been also estimated from a comparison to theoretical stellar evolutionary tracks. We have derived an age of 7 ± 3 Gyr from a Bayesian approach (del Burgo & Allende Prieto 2018) using the stellar evolution library PARSEC v1.2S, taking as input the iron-to-hydrogen ratio ([Fe/H] = −0.55 ± 0.17), the colour $r - J$ (determined from SDSS r and 2MASS J bands), and absolute magnitude M_J (calculated from 2MASS J and *Gaia* DR2 parallax), and their uncertainties.

According to our kinematic analysis (Cortés Contreras 2016) with U, V, and W velocities revised with the latest *Gaia* DR2 astrometry and our radial velocity, we conclude that Teegarden's Star belongs to an evolved population of the Galaxy, probably the thick disc. This is consistent with our age estimates.

In summary, Teegarden's Star is relatively magnetically quiet for its spectral type M7.0 V. Most late-M dwarfs known show higher levels of magnetic activity. Different approaches (Hα, X-ray, $v \sin i$, evolutionary track, and space motions) are compatible with the conclusion that Teegarden's Star is most likely a very old (8–10 Gyr) and very slowly rotating star ($P_{\rm rot} \gtrsim$ 100 d).

2.3. Transit visibility zones

The ecliptic latitude of Teegarden's Star is only 0.30 deg, which means that the star is very close to the plane of Earth's orbit around the Sun. An observer within a band of ±0.25 deg could see the Earth transiting in front of our Sun (Wells et al. 2018). Currently, Teegarden's Star is outside the transit bands of Earth and Mars, while Mercury has already been visible in transit since 1956 (Fig. 2). However, accounting for the fast stellar proper motion (it has the 15th largest proper motion, Wenger et al. 2000), we derive that Teegarden's Star will move into the transit band of Earth in 2044 and into that of Mars in 2190. For more than 200 yr, these three planets will exhibit transits as seen from Teegarden's Star. This is also the maximum number of solar system planets that can be simultaneously observed in transit. In about 2438, the Mars transits will stop, and slightly later, in 2496, there will be the last transit of Earth, while Mercury will stay in total for a millennium until 2872 in the transit visibility zone. Over the next 1000 yr, the transits of Venus, Jupiter, Saturn, and Neptune will be observable from Teegarden's Star (Fig. 2).

According to Wells et al. (2018), the probability of falling within the overlapping transit zones of Mercury, Earth, and Mars is 2.1 × 10^{-4}. So far, there is only one known exoplanet (K2-101 b, Barros et al. 2016; $R = 2\,R_\oplus$, Mann et al. 2017) within three overlapping transit zones (Jupiter, Saturn, and Uranus).

3. Observations

3.1. CARMENES spectra

The CARMENES instrument consists of a visual (VIS) and a near-infrared (NIR) spectrograph covering 520–960 nm and

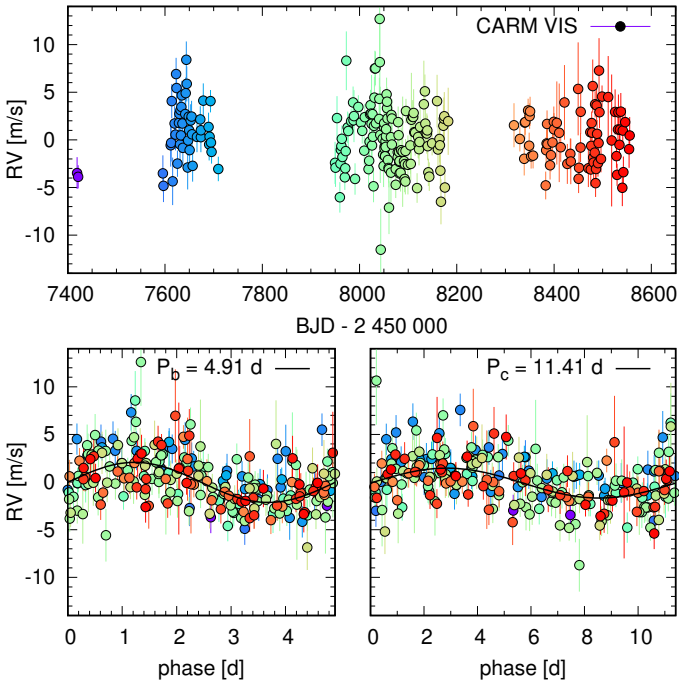

Fig. 3. *Top panel*: CARMENES RV time series for Teegarden's Star colour-coded with time. *Bottom panel*: RVs phase-folded to the periods of planets b (*left*) and c (*right*). In each case the contribution of the other planet was subtracted.

960–1710 nm with a spectral resolution of 94 600 and 80 400, respectively (Quirrenbach et al. 2014, 2018). It is located at the 3.5 m Zeiss telescope at the Centro Astronómico Hispano-Alemán (Almería, Spain). Since the start of CARMENES in January 2016, we obtained 245 spectra of Teegarden's Star within the CARMENES guaranteed time observations (GTO) survey for exoplanets (Reiners et al. 2018). The spectra have typical signal-to-noise ratios (S/Ns) of 58 per pixel around 746 nm (see also Fig. 1) and exposure times of 30 min. We extracted the spectra with the CARACAL pipeline, based on flat-relative optimal extraction (Zechmeister et al. 2014) and wavelength calibration that was performed by combining hollow cathode lamps (U-Ar, U-Ne, and Th-Ne) and Fabry-Pérot etalons (Bauer et al. 2015; Schäfer et al. 2018). The instrument drift during the nights is tracked with the Fabry-Pérot in the simultaneous calibration fibre.

We derived the radial velocities from the spectra with the SERVAL[8] code (Zechmeister et al. 2018). The data were corrected for nightly zero-point offsets, which were determined using a large set of RV standard stars from the GTO sample as described in Trifonov et al. (2018) and Tal-Or et al. (2019). These corrections were about 3 m s^{-1} at the beginning of the survey and 1 m s^{-1} after instrumental improvements (e.g. fibre coupling). Figure 3 (top) shows the RV time series.

3.2. Photometry

Complementary to the spectroscopic data, we also obtained our own and archival photometric data from various instruments. On one hand, the photometric data were used to estimate the rotation period of Teegarden's Star from (quasi-)periodic brightness variations (Sect. 5.1). On the other hand, we searched for transits (Sect. 5.2) guided by the orbital solutions from the RV analysis. In Appendix A we briefly describe the seven instruments whose

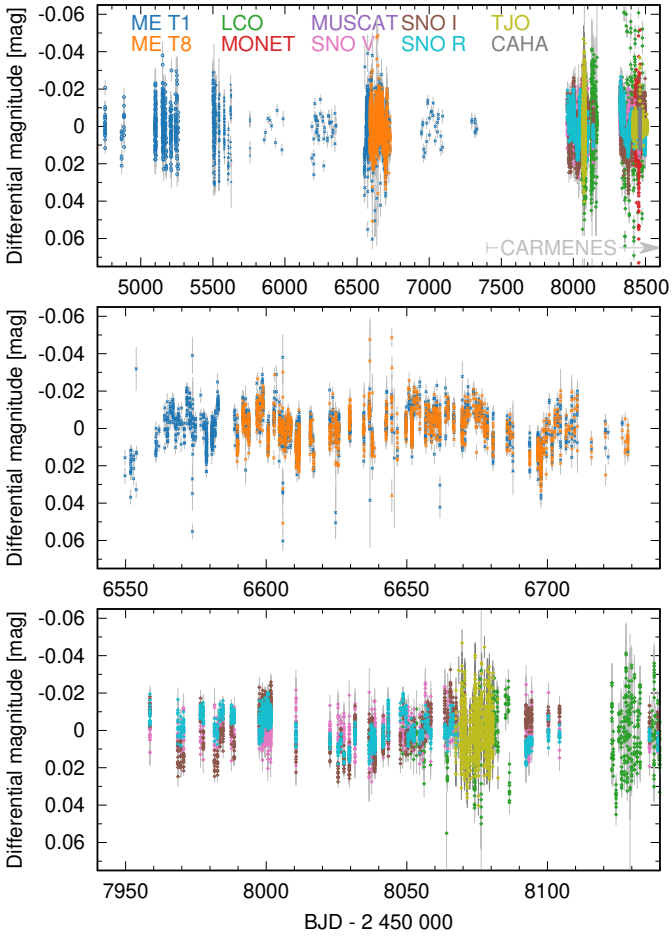

Fig. 4. Photometry from different instruments and bands (*top*) with 200 d zooms to MEarth data (*middle*) and LCO, SNO, and TJO data from 2017 (*bottom*).

basic properties are summarised in Table A.1. Figure 4 and Table A.2 provide an overview of the available photometric data, temporal sampling, and precision. As explained in Sect. 5.1, we removed the strongest signal in each data set after the non-detection of a common periodicity for all data sets. This assumes that the strongest peak is due to remaining systematic effects.

All CCD measurements were obtained by the method of synthetic aperture photometry using typically 2 × 2 binning. Each CCD frame was corrected in a standard way for bias, dark, and flat field by instrument-specific pipelines. From a number of nearby and relatively bright stars within the frames, the best sets were selected as reference stars.

4. Spectroscopic data analysis

4.1. Radial velocities and orbit parameters

We secured 245 spectra with CARMENES. Seven spectra without simultaneous Fabry-Pérot drift measurements are excluded from the RV analysis. This leaves 238 RVs that cover a time span of 1136 d (Fig. 3, top panel). The effective data uncertainty $(\sum \sigma_i^{-2}/N)^{-0.5}$ is 1.67 m s^{-1} and the weighted root-mean-square (rms) is 2.82 m s^{-1}, leaving an unexplained noise (stellar jitter, calibration noise, or planetary signals) of 2.19 m s^{-1}.

The GLS periodogram[9] (Zechmeister & Kürster 2009) of the RVs (Fig. 5, top) shows two strong peaks at P_b = 4.910 d and

[8] https://github.com/mzechmeister/serval

[9] https://github.com/mzechmeister/GLS

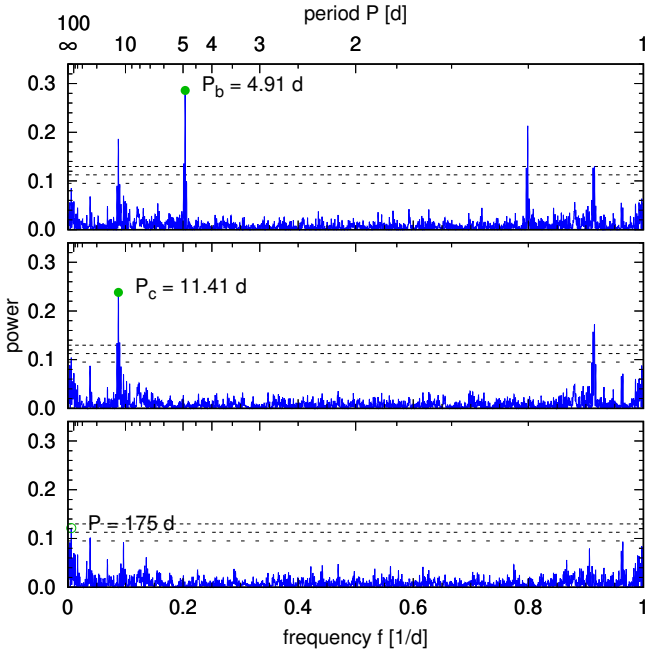

Fig. 5. GLS periodogram of the RVs (*top*), after subtraction of the first signal P_b (*middle*), and after subtraction of the second signal P_c (residuals, *bottom*). Horizontal lines indicate the 1, 0.1, and 0.01 % FAP levels.

$P'_b = 1.25$ d, which are related to each other by the typical one-day aliasing ($1/P'_b = 1/\mathrm{d} - 1/P_b$). The 4.910 d period is clearly preferred (analytical false-alarm probability $\mathrm{FAP}_b = 8.1 \times 10^{-15}$ versus $\mathrm{FAP}'_b = 5.9 \times 10^{-10}$). In Fig. 3 (bottom left) the RVs are phase-folded to period P_b and corrected for the contribution of a second signal P_c (see below).

The residuals after subtraction of the signal P_b shows a further peak at $P_c = 11.41$ d (Fig. 5, middle panel) with an $\mathrm{FAP} = 1.6 \times 10^{-11}$. The RVs are folded to this period in Fig. 3 (bottom right). After subtracting the signal P_c, the periodogram has the highest peak at a (probably spurious) 175 d period (Fig. 5, bottom). The signal at $P_d = 25.94$ d ($K_d = 0.9\,\mathrm{m\,s^{-1}}$) deserves further attention. It reaches an FAP = 0.5 % and requires more data for confirmation.

We modelled the RVs with two Keplerian signals. We chose an additive noise term (jitter σ_{jit}) to encompass further unmodelled sources (e.g. stellar activity, further planets, and additional instrumental or observational errors) that could be present in our data. The jitter was added in quadrature to the data uncertainties, which thereby re-weighted the data and balanced between a weighted and an unweighted fit (in case of $\sigma_{\mathrm{jit}} = 0$ and $\sigma_{\mathrm{jit}} \to \infty$, respectively). The ten Keplerian parameters, the RV zero-point, and the jitter term were optimised by maximising a Gaussian likelihood. We used uniform priors for all parameters and explored the posteriors with a Markov chain Monte Carlo (MCMC) method (`emcee`, Foreman-Mackey et al. 2013) as well as with the curvature matrix.

Figure C.1 shows the posterior distribution for the Keplerian parameters from 500 000 samples. Their medians and 1σ uncertainties (estimated from equal-tailed 50th–16th and 84th–50th percentile spreads) are summarised in Table 2. The covariance matrix, which was obtained by fitting a 12-dimensional paraboloid[10] to the 150 best samples with the highest likelihood values, provides similar estimates as indicated by the error ellipses. The covariance matrix can handle only linear correlations. The amplitudes are $K_b = 2.0\,\mathrm{m\,s^{-1}}$ and $K_c = 1.6\,\mathrm{m\,s^{-1}}$; the weighted rms is $2.06\,\mathrm{m\,s^{-1}}$ (best sample), and the jitter is $1.21\,\mathrm{m\,s^{-1}}$.

[10] https://github.com/mzechmeister/serval/blob/master/src/paraboloid.py

Table 2. Orbital planet and statistical parameters of Teegarden's Star b and c.

Keplerian parameters	Planet b	Planet c
P (d)	$4.9100^{+0.0014}_{-0.0014}$	$11.409^{+0.009}_{-0.009}$
K ($\mathrm{m\,s^{-1}}$)	$2.02^{+0.19}_{-0.20}$	$1.61^{+0.19}_{-0.19}$
e [(a)]	$0.00^{+0.16}$	$0.00^{+0.16}$
ω (deg)	77^{+52}_{-79}	286^{+101}_{-74}
$t_p - 2\,458\,000$ (d)	$52.3^{+0.7}_{-1.1}$	$53.2^{+3.2}_{-2.3}$
Derived parameters		
a (au)	$0.0252^{+0.0008}_{-0.0009}$	$0.0443^{+0.0014}_{-0.0015}$
$m \sin i$ ($M_\oplus$)	$1.05^{+0.13}_{-0.12}$	$1.11^{+0.16}_{-0.15}$
m ($M_\oplus$) [(b)]	$1.25^{+0.68}_{-0.22}$	$1.33^{+0.71}_{-0.25}$
$\sin i$ [(b)]	$0.87^{+0.12}_{-0.31}$	
F ($S_\oplus$) [(c)]	$1.15^{+0.08}_{-0.08}$	$0.37^{+0.03}_{-0.03}$
Statistical parameters		
N	238	
T (d)	1136	
Internal uncertainties ($\mathrm{m\,s^{-1}}$)	1.67	
Jitter ($\mathrm{m\,s^{-1}}$)	$1.21^{+0.16}_{-0.16}$	
wrms ($\mathrm{m\,s^{-1}}$)	2.06	
$\ln L$	−520.98	
$\Delta \ln L$	69.16	

Notes. [(a)]One-side distributed; 68 % interval. [(b)]For geometrically randomly oriented orbits (uniform distribution in $\cos i$). [(c)]Insolation with stellar parameters adopted from Schweitzer et al. (2019).

Both orbits are circular within the eccentricity uncertainties. The eccentricity posteriors cumulate near zero and have a one-sided distribution. Therefore, we give a 68% percentile in Table 2. In case of low eccentricities, the time of periastron passage t_p and periastron longitude ω are degenerate. Therefore, both parameters are poorly constrained, as indicated by their broad distribution, in particular for planet c. To preserve the phase information, which is encoded in their strong correlation (coefficients of 0.9987 and 0.985 in the covariance matrix), we provide a time of inferior conjunction t_{ic} (i.e. a potential transit time t_{tr}) derived from the samples (Fig. C.2). These transit times have smaller uncertainties than does the time of periastron passage.

From the Keplerian parameters, we derived planetary minimum masses using a Gaussian prior for the stellar mass (Fig. C.3; because the stellar mass is not constrained by the likelihood, the posterior matches the prior). The minimum masses are $m_b \sin i = 1.05\ M_\oplus$ and $m_c \sin i = 1.11\ M_\oplus$. To estimate true masses, we further drew for each sample an inclination from a uniform distribution of $\cos i$, which corresponds to geometrically random orientations (Kürster et al. 2008). The median values of the true masses are around 16% higher than the minimum masses ($\cos i = 0.5 \to 1/\sin i = 1.155$).

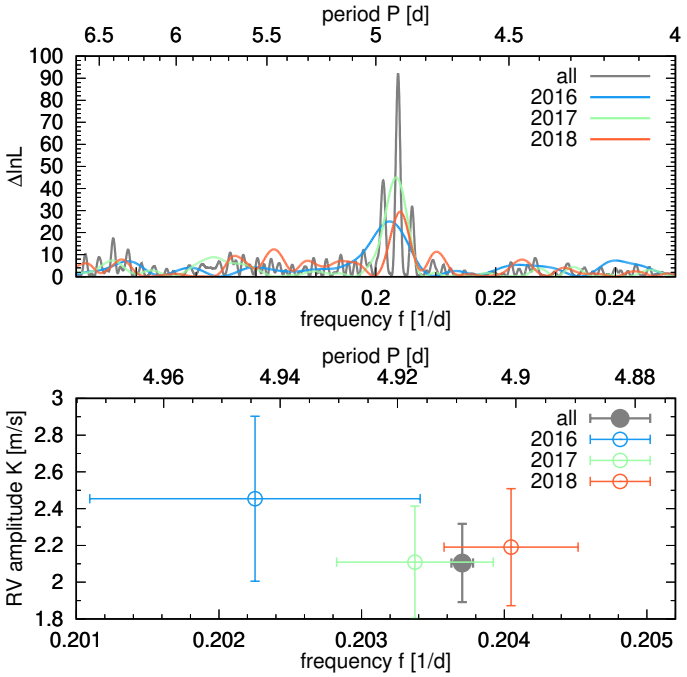

Fig. 6. *Top panel*: GLS periodograms around P_b for three CARMENES seasons (same colour-coding as in Fig. 3). *Bottom panel*: RV amplitude and period of the highest peaks along with uncertainty estimates. The grey curve and (filled) symbol corresponds to the joint data set.

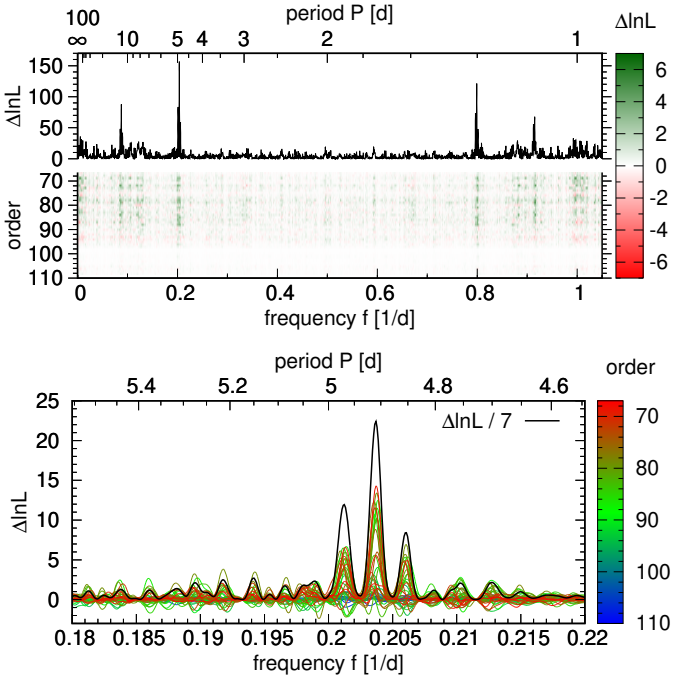

Fig. 7. *Top panel*: total maximum likelihood periodogram for the order-wise RVs (black curve) and an order-frequency map colour-coded by the likelihood contribution. *Bottom panel*: zoom-in to the period P_b and colour-coding with the echelle order. For the sake of clarity, the total likelihood (black curve) is downscaled by a factor 7.

In the following sections we analyse the RV data in more detail. We also investigate further activity indicators to determine whether we can attribute both signals to a planetary origin.

4.2. Temporal coherence of the RV signal

We subdivided the RV data into the three seasons to analyse the stability of the RV signal. We computed for each season the best-fitting period and amplitude (Fig. 6). As expected, the parameter uncertainties increase due to the smaller number of data points (2016: 44, 2017: 125, and 2018: 67). However, the amplitudes and periods between the seasons are all consistent within their 1σ uncertainties. This result indicates that the 4.91 d period is stable over at least 1000 d.

4.3. Chromatic coherence of the RV signal

The RV of each epoch is the average of individual RVs measured in 42 echelle orders. During this averaging, information about a possible wavelength dependence of the RV signal is lost. To check the contributions of the orders to a periodic signal, we here treated each order as an independent instrument. Therefore, we fit for a fixed trial frequency f a sine simultaneously to all orders with one common amplitude and phase. Each order o has its own offset μ_o and jitter term σ_o. We optimised the parameters by maximising the total likelihood

$$\ln L = \sum_o \ln L_o, \tag{1}$$

where the likelihood for one order summed over all epochs n is

$$\ln L_o = -\frac{1}{2} \sum_n \ln 2\pi(\sigma_{n,o}^2 + \sigma_o^2) + \frac{[\mathrm{RV}_{n,o} - \mathrm{RV}(t_{n,o}) - \mu_o]^2}{\sigma_{n,o}^2 + \sigma_o^2}, \tag{2}$$

with the model $\mathrm{RV}(t) = a \cos \tau f t + b \sin \tau f t$. By looping over a sequence of frequencies f_k, we computed a maximum likelihood periodogram. Figure 7 shows the likelihood improvement with respect to the likelihood L_0 of a constant model ($a = b = 0$),

$$\Delta \ln L = \ln L - \ln L_0 = \sum_o \ln L_o - \sum_o \ln L_{0,o} = \sum_o \Delta \ln L_o. \tag{3}$$

The evaluation of this maximum likelihood periodogram takes much longer than the GLS periodogram because there are many more parameters (including non-linear jitter terms).

The contributions of the orders can of course be of different strengths and depend on their RV information content, as well as their S/N. The log-likelihood change of individual orders can be even negative when the period in such an order has an amplitude or phase that is significantly different from the rest. However, the total log-likelihood change cannot be negative in this simultaneous approach ($\Delta \ln L \geq 0$). In Fig. 7 no order significantly contradicts ($\Delta \ln L_o > -2$) at P_b, so the orders contribute in a positive way, as expected for a planetary signal.

4.4. Near-infrared radial velocities

In Reiners et al. (2018) we showed with CARMENES data that M dwarfs have a lower RV content in the NIR than expected from previous predictions (e.g. Reiners et al. 2010; Rodler et al. 2011). Coupled with the current instrument and pipeline performance, the NIR RVs of Teegarden's Star have a weighted rms of 5.75 m s^{-1}, making the detection of 1–2 m s^{-1} signals difficult. Still, signals with P_b and P_c are the highest peaks in the GLS periodogram of the NIR RVs (Fig. 8). The formal FAP of P_b is 0.1%, that is, significant. The small signal at P_d in the VIS RVs is not seen in the NIR RVs, however.

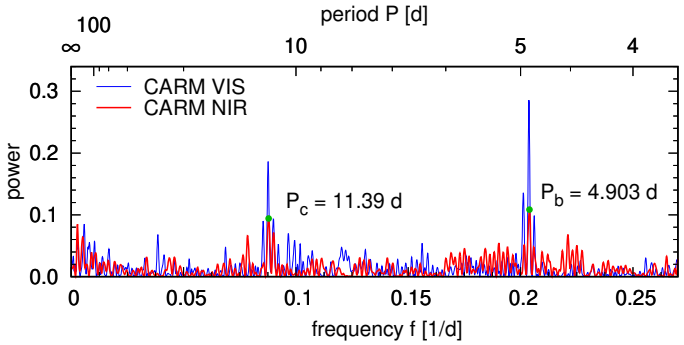

Fig. 8. GLS periodogram of NIR RVs compared to VIS RVs.

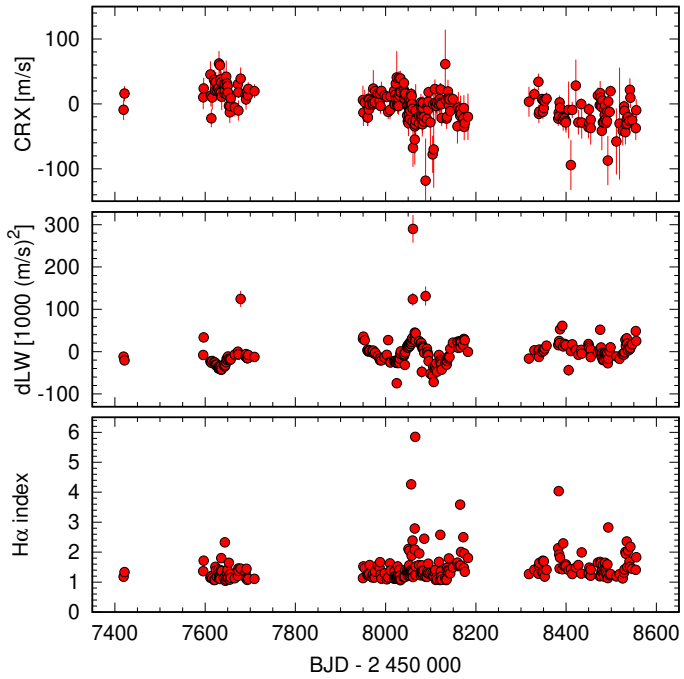

Fig. 9. Time series of the activity indicators: chromatic index CRX (*top*), differential line width dLW (*middle*), and Hα index (*bottom*).

4.5. Activity indicators

We extracted three activity indicators from the CARMENES spectra as described in Zechmeister et al. (2018). The time series of the chromatic index (CRX), the differential line width (dLW), and the Hα index are shown in Fig. 9 and their periodograms in Fig. B.1.

The CRX time series has some negative excursions around BJD $-2\,450\,000 = 8050-8100$, which coincides with dLW excess and also increased Hα activity. During this time, the largest Hα emission occurred (Fig. 1). We see no clear periodicity for CRX (Fig. 10). The highest periodogram peak is at 1000 d, which captures the slight trend. After its removal, the highest peak is at 120 d, which captures the previous feature of increased Hα activity. No power is found at the planet periods during this pre-whitening. This result agrees with the analysis from Sect. 4.3, which exploits the wavelength-dependent information in a different way.

The differential line width (dLW) as well as the full width at half-maximum (FWHM) or contrast are also used as activity indicators. However, they can be also affected by instrumental and observational effects, such as focus change of the spectrograph, sky-background, or broadening due to differential barycentric motion. We realised that dLW outliers are indeed caused by a close Moon separation during cloudy nights, which leads to an increased sky background. Ignoring these points, dLW is dominated by long-term variations, but it is not clear whether their origin is related to stellar rotation. The dLW has no power at the two RV periods (Fig. 10).

The Hα time series shows a few flare events. Even after excluding them, we see no power at the RV periods (Fig. 10).

5. Photometry analysis

As mentioned in Sect. 3.2, we collected photometric data for two purposes. First, we wished to rule out that the RV signals are due to stellar rotation. Second, the small stellar radius allows a ground-based transit search down to Earth-size planets, which is the expected radius range of the two planets.

Unfortunately, Teegarden's Star was not observed by the *Kepler* space telescope (Borucki et al. 2010), although it broadly covered the ecliptic during its *K2* mission. Moreover, Teegarden's Star is not included in the scheduling plan of the Transiting Exoplanet Survey Satellite mission (TESS, Ricker et al. 2015), which excludes ecliptic latitudes below 6 deg.

Because Teegarden's Star is very red, ground-based photometry suffers from quite severe colour effects: all comparison stars are bluer. Prior to an analysis, we therefore detrended all the photometric data. MEarth data offer the possibility for detrending using additional information, such as CCD position, airmass, or the so-called common mode (a kind of detrended differential magnitude corrected for main known systematic effects)[11]. We investigated possible detrending options and decided for a final data set using the position of the star on the CCD and the common mode. For a consistency check, we also used the original data. Our own data were detrended using either airmass or night-by-night polynomial fits.

Despite these corrections, we analysed the various data sets individually because the different filters, CCD sensitivities, and comparison stars very likely lead to systematic differences in possible activity-induced photometric signals. Only the MEarth data were also combined into a seven-year-long light curve (excluding the 2010–2011 data using the $I_{715-895}$ interference filter).

5.1. Rotation period

Because a measured rotation period is not available (Sect. 2.2), we re-analysed all available data (Table A.2, Fig. 4) using GLS periodograms. There is no common periodicity detectable that were present in all data or even in a sub-set. The combined original MEarth data indicate a period at 5.11 d. The TJO data periodogram also shows a peak at this period, but not as the strongest one. In the de-trended MEarth data, this period is not detectable, however. Two data sets (MEarth from 2014 and LCO) show a 28 d periodicity that we attribute to uncorrected Moon contamination. A common property of most data sets is a periodicity between 50 and 80 d. This might be an indication of a rotation period in that range, but it is below our detection threshold, probably due to a combination of aliasing and short lifetimes of active regions (shorter than this possible rotation period).

Assuming that the various periodicities in our photometric data are due to uncorrected systematics, we removed the largest

[11] https://www.cfa.harvard.edu/MEarth/DataDR7.html

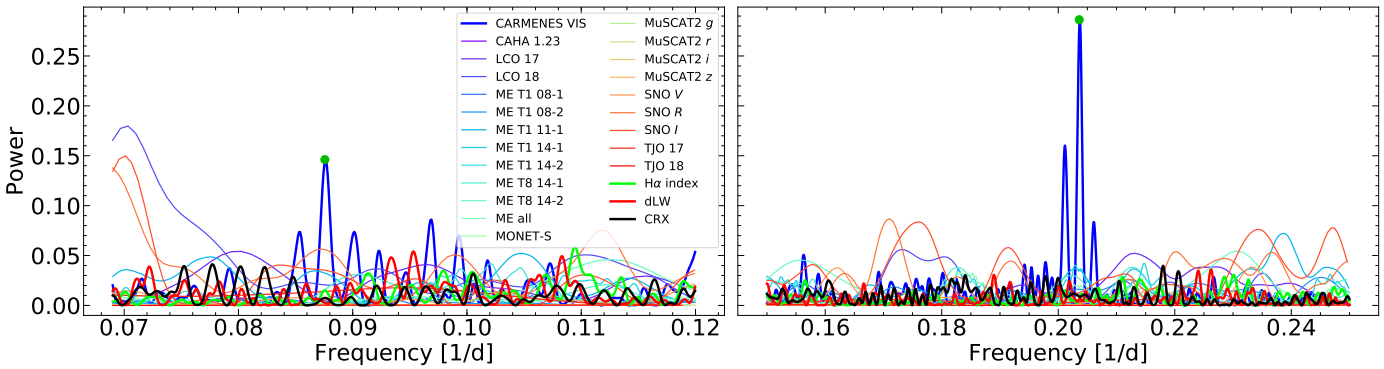

Fig. 10. GLS periodograms of photometry and various activity indicators compared to CARMENES VIS RVs (thick blue line) around P_c (*left panel*) and P_b (*right panel*).

signal from each data set using a sinusoidal fit. In the pre-whitened data, a weak rotation period may become detectable. However, a common period in the photometric data is again lacking. As demonstrated in Fig. 10, there is no significant period at one of the two planet orbital periods.

We conclude that we cannot detect a rotation period in Teegarden's Star. The photometric non-detection could indicate a long stellar rotation period resulting in small amplitudes and relatively short lifetimes of active regions. Neither activity indicators nor photometry contradict the interpretation of the two RV signals as being due to planets.

5.2. Transit search

The transit probability of planet b is $p_{\rm tr,b} \approx R_\star/a_{\rm b} \approx 2.1\%$, and its maximum transit depth would be up to $R_{\rm b}^2/R_\star^2 \approx 0.7\%$ with a transit duration of $\Delta t_{\rm b} \lessapprox 40$ min. We focussed our follow-up on planet b because the transit probability of planet c is lower ($p_{\rm tr,c} = 1.1\%$), the transit duration is longer ($\Delta t_{\rm c} \lessapprox 60$ min), and it has fewer and more uncertain transit windows, which makes ground-based transit searches more challenging.

Our photometric data cover the potential transit phase of planet b densely. Figure 11 shows the photometric data phase-folded to $P_{\rm b}$. An example of an expected transit signal is overplotted. A combined fit of RV data and photometric data (including an offset and a jitter term for each photometric data set) does not indicate a transit signal, and neither does a box-least-squares search (Kovács et al. 2002) in the photometry. Because not all individual data sets cover the full orbital phase space and they have different photometric precision, an estimate of our detection limit is difficult to compute and would not be very reliable. A conservative estimate is a detection limit of 2 mmag for the depth of a transit signal over the full transit window of 1 d width.

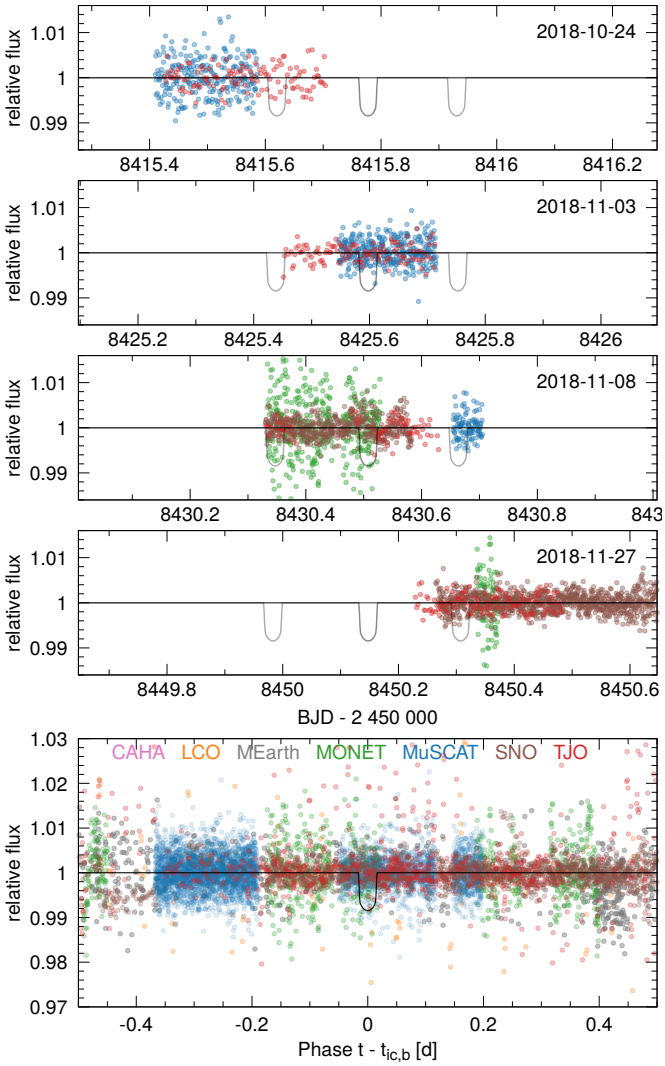

Fig. 11. Transit search with various de-trended photometric data sets. *Top panels*: four high-cadence nights from the transit search. The transit model (black curve) shows the expected signal for planet b and for maximum transit depth. The left and right models (grey) indicate the predicted 1σ uncertainty for the transit window (0.15 d, 3.6 h). *Bottom panel*: all photometric data phase-folded with $P_{\rm b}$ and $t_{\rm ic,b}$.

6. Discussion and conclusions

From the analysis we conclude that the two RV signals indicate the presence of two exoplanets. Despite the low amplitudes, the RV signals are significantly detected and have no counterpart, neither in the spectroscopic activity indicators nor in the extensive photometry available to us. Moreover, we have shown that the 4.9 d signal is stable over the three years of observations in period and amplitude.

Despite intensive monitoring, we cannot derive a rotation period. However, the low photometric variability, the moderate Hα emission, and the dLW and CRX indicators suggest a long rotation period. This is in contrast to many other late-M dwarfs, which are very active and rotate rapidly. We therefore conclude that Teegarden's Star is old and that the two signals at 4.91 and 11.4 d are best explained by the Keplerian motion of exoplanets.

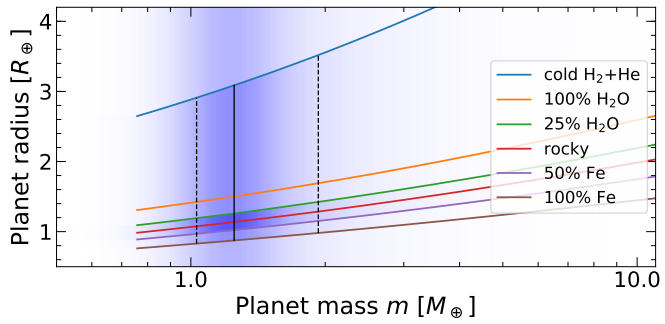

Fig. 12. Mass-radius relation for various compositions (Zeng et al. 2016). The probability for the true mass of planet b is horizontally shaded by the blue gradient; the vertical lines indicate the median (solid black) and 17 and 83% percentiles (dashed black). The region of less extreme compositions between 25% H_2O and 50% Fe is additionally highlighted.

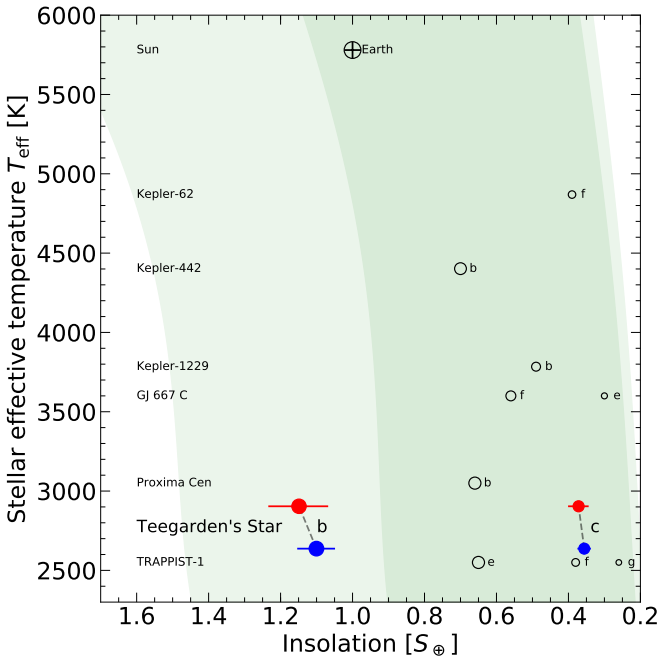

Fig. 13. Optimistic (light green) and conservative (dark green) habitable zone for 1 $M_\oplus$ according to Kopparapu et al. (2014). Teegarden's Star planets b and c are shown for two stellar parameter sets (red dots: Schweitzer et al. 2019; blue dots: Rojas-Ayala et al. 2012; Dieterich et al. 2014). The insolation error bar depicts the effect due to intrinsic uncertainty in $T_{\rm eff}$. For comparison, we plot nine planets (including Proxima b and TRAPPIST-1 e, f, and g) from the Habitable Exoplanet Catalog[12] (black circles) and the Earth (black circled plus) at the top. All symbol sizes scale with the fourth power of the Earth Similarity Index (ESI) assuming a rocky composition.

As a note of caution, the late spectral type of Teegarden's Star takes RV analyses into a quite unexplored regime where scaling relations between photometric and RV variations are not established. However, even if RVs turn out to be much more sensitive to stellar variability and one period is connected to stellar rotation, then at least the other signal should be a planet. Period ratios of 2:1 can be caused by the harmonics of stellar rotation (but also eccentric and resonant planets). However, the period ratio is $P_c/P_b = 2.32$, which is close to but noticeably different from 2:1. Such a discrepancy is hard to explain even with differential rotation, while departures from exact 2:1 ratios are often observed in exoplanet systems (Steffen & Hwang 2015).

Despite the low planetary masses, the dynamical interaction between the two planets is noticeable on longer timescales of decades but not on the rather short timescale of our observations. Using the N-body integrator implemented in Systemic (Meschiari et al. 2009), we integrated the orbits for up to 10^5 yr. It should be noted that the eccentricity changes periodically by about $\Delta e/\mathrm{median}(e) \approx 30\%$ on timescales of about 2000 yr, while the periods are stable within about $\Delta P/\mathrm{median}(P) < 0.0003$.

Because no transits are detected, we cannot derive the planetary radii. We therefore estimated them from mass-radius relations for various compositions (Zeng et al. 2016). The planetary radii depend weakly on the planetary mass, but strongly on the bulk composition (Fig. 12). Between the two extreme compositions, namely a pure Fe core on the one side and a cold H+He mini-Neptune on the other, the radii differ by a factor of about three (see Fig. 12). We used these radii as well as other stellar and planetary parameters to derive the Earth Similarity Index (ESI) as defined by Schulze-Makuch et al. (2011). The ESI is an indicator that compares key parameters to those of our Earth ($\mathrm{ESI}_\oplus = 1$). Here we used the weighted ESI, taking into account the equilibrium temperature, atmospheric escape velocity, bulk density, and radius, with a dominant contribution from the equilibrium temperature. The weights were taken from the Habitable Exoplanet Catalog[12]. Except for the case of a mini-Neptune composition, the two planets have a high ESI. For a potentially rocky composition, the ESI value is 0.94 and 0.8 for planets b and c, respectively. This makes Teegarden's Star b the planet with currently the highest ESI value. However, the ESI is only an estimate, and different weighting of the parameters may lead to changing ESIs. This ESI definition, for example, does not take into account the stellar spectral energy distribution and the resulting planetary atmospheric composition, which very likely have an effect on habitability.

We displayed the two planets of Teegarden's Star (see Fig. 13) with nine other Earth-like planets within the conservative habitable zone (HZ) listed in the Habitable Exoplanet Catalog and compared their incident stellar flux with their position relative to the HZ according to Kopparapu et al. (2014) as a function of stellar effective temperature. We also took the different stellar parameters for Teegarden's Star into account. Planet b is placed just outside the hot end of the conservative HZ (but inside the optimistic one), whereas planet c is comfortably within this zone. In addition, planet b receives nearly the same stellar flux as the Earth and therefore has a nearly identical equilibrium temperature, but is outside the conservative HZ. As discussed by Kopparapu et al. (2014), this is caused by a runaway greenhouse effect that is due to water vapour starting at lower insolation for low-mass stars. This effect is neglected in the ESI calculation and leads to the curious fact that planet b has a higher ESI value than planets inside the conservative HZ.

The planets in this planetary system, especially Teegarden's Star c, could become prime targets for further characterisation with the next generation of extremely large telescopes (ELTs). Some of the planned instruments, such as the Planetary Systems Imager (PSI, Guyon et al. 2018) for the Thirty Meter Telescope (TMT), aim to achieve contrast values of 10^{-7} at ~0.01 arcsec. Assuming Earth-size for Teegarden's Star c, the contrast ratio of the reflected light from the planet is also expected to be of the order of 10^{-7} at the projected angle of the semi-major

[12] http://phl.upr.edu/projects/habitable-exoplanets-catalog

axis of ~0.012 arcsec. Thus, high-contrast imagers for the new ELTs, both in the Northern and Southern Hemispheres, now have additional motivation because they can stand a good chance of directly imaging nearby and potentially habitable Earth-mass planets. This will enable a detailed study of their properties.

The exoplanet system around Teegarden's Star is a pioneering discovery by the CARMENES survey and remarkable in several aspects. The planets Teegarden's Star b and c are the first planets detected with the RV method around such an ultra-cool dwarf. Both planets have a minimum mass close to one Earth mass, and given a rocky, partially iron, or water composition, they are expected to have Earth-like radii. Additionally, they are close to or within the conservative HZ, or in other words, they are potentially habitable. Our age estimate of 8 Gyr implies that these planets are about twice as old as the solar system. Interestingly, our solar system currently is within the transit zone as seen from Teegarden's Star. For any potential Teegardians, the Earth will be observable as a transiting planet from 2044 until 2496.

Acknowledgements. We thank the referee Rodrigo Díaz for a careful review and helpful comments. M.Z. acknowledges support from the Deutsche Forschungsgemeinschaft under DFG RE 1664/12-1 and Research Unit FOR2544 "Blue Planets around Red Stars", project no. RE 1664/14-1. CARMENES is an instrument for the Centro Astronómico Hispano-Alemán de Calar Alto (CAHA, Almería, Spain). CARMENES is funded by the German Max-Planck-Gesellschaft (MPG), the Spanish Consejo Superior de Investigaciones Científicas (CSIC), the European Union through FEDER/ERF FICTS-2011-02 funds, and the members of the CARMENES Consortium (Max-Planck-Institut für Astronomie, Instituto de Astrofísica de Andalucía, Landessternwarte Königstuhl, Institut de Ciències de l'Espai, Institut für Astrophysik Göttingen, Universidad Complutense de Madrid, Thüringer Landessternwarte Tautenburg, Instituto de Astrofísica de Canarias, Hamburger Sternwarte, Centro de Astrobiología and Centro Astronómico Hispano-Alemán), with additional contributions by the Spanish Ministry of Economy, the German Science Foundation through the Major Research Instrumentation Programme and DFG Research Unit FOR2544 "Blue Planets around Red Stars", the Klaus Tschira Stiftung, the states of Baden-Württemberg and Niedersachsen, and by the Junta de Andalucía. Based on data from the CARMENES data archive at CAB (INTA-CSIC). This article is based on observations made with the MuSCAT2 instrument, developed by ABC, at Telescopio Carlos Sánchez operated on the island of Tenerife by the IAC in the Spanish Observatorio del Teide. Data were partly collected with the 150-cm and 90-cm telescopes at the Sierra Nevada Observatory (SNO) operated by the Instituto de Astrofísica de Andalucía (IAA-CSIC). Data were partly obtained with the MONET/South telescope of the MOnitoring NEtwork of Telescopes, funded by the Alfried Krupp von Bohlen und Halbach Foundation, Essen, and operated by the Georg-August-Universität Göttingen, the McDonald Observatory of the University of Texas at Austin, and the South African Astronomical Observatory. We acknowledge financial support from the Spanish Agencia Estatal de Investigación of the Ministerio de Ciencia, Innovación y Universidades and the European FEDER/ERF funds through projects AYA2015-69350-C3-2-P, AYA2016-79425-C3-1/2/3-P, AYA2018-84089, BES-2017-080769, BES-2017-082610, ESP2015-65712-C5-5-R, ESP2016-80435-C2-1/2-R, ESP2017-87143-R, ESP2017-87676-2-2, ESP2017-87676-C5-1/2/5-R, FPU15/01476, RYC-2012-09913, the Centre of Excellence "Severo Ochoa" and "María de Maeztu" awards to the Instituto de Astrofísica de Canarias (SEV-2015-0548), Instituto de Astrofísica de Andalucía (SEV-2017-0709), and Centro de Astrobiología (MDM-2017-0737), the Generalitat de Catalunya through CERCA programme", the Deutsches Zentrum für Luft- und Raumfahrt through grants 50OW0204 and 50OO1501, the European Research Council through grant 6 94 513, the Italian Ministero dell'instruzione, dell'università de della ricerca and Università degli Studi di Roma Tor Vergata through FFABR 2017 and "Mission: Sustainability 2016", the UK Science and Technology Facilities Council through grant ST/P000592/1, the Israel Science Foundation through grant 848/16, the Chilean CONICYT-FONDECYT through grant 31 80 405, the Mexican CONACYT through grant CVU 4 48 248, the JSPS KAKENHI through grants JP18H01265 and 18H05439, and the JST PRESTO through grant JPMJPR1775.

References

Alonso-Floriano, F. J., Morales, J. C., Caballero, J. A., et al. 2015, A&A, 577, A128
Anglada-Escudé, G., Amado, P. J., Barnes, J., et al. 2016, Nature, 536, 437
Barnes, S. A. 2007, ApJ, 669, 1167
Barros, S. C. C., Demangeon, O., & Deleuil, M. 2016, A&A, 594, A100
Bauer, F. F., Zechmeister, M., & Reiners, A. 2015, A&A, 581, A117
Berta, Z. K., Irwin, J., Charbonneau, D., Burke, C. J., & Falco, E. E. 2012, AJ, 144, 145
Borucki, W. J., Koch, D., Basri, G., et al. 2010, Science, 327, 977
Caballero, J. A., Cortés-Contreras, M., Alonso-Floriano, F. J., et al. 2016, 19th Cambridge Workshop on Cool Stars, Stellar Systems, and the Sun (CS19), 148
Collins, K. A., Kielkopf, J. F., Stassun, K. G., & Hessman, F. V. 2017, AJ, 153, 77
Colome, J., & Ribas, I. 2006, IAU Spec. Sess., 6, 11
Cortés Contreras, M. 2016, PhD Thesis, Universidad Complutense de Madrid, Madrid, Spain
del Burgo, C., & Allende Prieto, C. 2018, MNRAS, 479, 1953
Dieterich, S. B., Henry, T. J., Jao, W.-C., et al. 2014, AJ, 147, 94
Donati, J.-F., Kouach, D., Lacombe, M., et al. 2018, SPIRou: A NIR Spectropolarimeter/High-Precision Velocimeter for the CFHT (Cham: Springer International Publishing), 107
Foreman-Mackey, D., Hogg, D. W., Lang, D., & Goodman, J. 2013, PASP, 125, 306
Gaia Collaboration (Brown, A. G. A., et al.) 2018, A&A, 616, A1
Gatewood, G., & Coban, L. 2009, AJ, 137, 402
Gillon, M., Jehin, E., Lederer, S. M., et al. 2016, Nature, 533, 221
Gillon, M., Triaud, A. H. M. J., Demory, B.-O., et al. 2017, Nature, 542, 456
Guyon, O., Mazin, B., Fitzgerald, M., et al. 2018, Proc. SPIE, 10703, 107030Z
Henden, A. A., Levine, S., Terrell, D., & Welch, D. L. 2015, AAS Meeting Abstracts, 225, 336.16
Husser, T.-O., Wende-von Berg, S., Dreizler, S., et al. 2013, A&A, 553, A6
Irwin, J., & Bouvier, J. 2009, IAU Symp., 258, 363
Jeffers, S. V., Schöfer, P., Lamert, A., et al. 2018, A&A, 614, A76
Kopparapu, R. K., Ramirez, R. M., SchottelKotte, J., et al. 2014, ApJ, 787, L29
Kotani, T., Tamura, M., Nishikawa, J., et al. 2018, Proc. SPIE, 10702, 1070211
Kovács, G., Zucker, S., & Mazeh, T. 2002, A&A, 391, 369
Kürster, M., Endl, M., & Reffert, S. 2008, A&A, 483, 869
Mahadevan, S., Ramsey, L. W., Terrien, R., et al. 2014, Proc. SPIE, 9147, 91471G
Mann, A. W., Gaidos, E., Vanderburg, A., et al. 2017, AJ, 153, 64
McCully, C., Volgenau, N. H., Harbeck, D.-R., et al. 2018, Proc. SPIE, 10707, 107070K
Meschiari, S., Wolf, A. S., Rivera, E., et al. 2009, PASP, 121, 1016
Narita, N., Fukui, A., Kusakabe, N., et al. 2019, J. Astron. Telesc., Instrum. Syst., 5, 015001
Newton, E. R., Irwin, J., Charbonneau, D., et al. 2016, ApJ, 821, 93
Newton, E. R., Irwin, J., Charbonneau, D., et al. 2017, ApJ, 834, 85
Passegger, V. M., Reiners, A., Jeffers, S. V., et al. 2018, A&A, 615, A6
Quirrenbach, A., Amado, P. J., Caballero, J. A., et al. 2014, Proc. SPIE, 9147, 91471F
Quirrenbach, A., Amado, P. J., Ribas, I., et al. 2018, Proc. SPIE, 10702, 107020W
Reiners, A., & Basri, G. 2010, ApJ, 710, 924
Reiners, A., Bean, J. L., Huber, K. F., et al. 2010, ApJ, 710, 432
Reiners, A., Schüssler, M., & Passegger, V. M. 2014, ApJ, 794, 144
Reiners, A., Zechmeister, M., Caballero, J. A., et al. 2018, A&A, 612, A49
Ricker, G. R., Winn, J. N., Vanderspek, R., et al. 2015, J. Astron. Telesc., Instrum. Syst., 1, 014003
Rodler, F., Del Burgo, C., Witte, S., et al. 2011, A&A, 532, A31
Rodríguez, E., García, J. M., Costa, V., et al. 2010, MNRAS, 408, 2149
Rojas-Ayala, B., Covey, K. R., Muirhead, P. S., & Lloyd, J. P. 2012, ApJ, 748, 93
Schäfer, S., Guenther, E. W., Reiners, A., et al. 2018, Proc. SPIE, 10702, 1070276
Schulze-Makuch, D., Méndez, A., Fairén, A. G., et al. 2011, Astrobiology, 11, 1041
Schweitzer, A., Passegger, V. M., Cifuentes, C., et al. 2019, A&A, 625, A68
Skrutskie, M. F., Cutri, R. M., Stiening, R., et al. 2006, AJ, 131, 1163
Steffen, J. H., & Hwang, J. A. 2015, MNRAS, 448, 1956
Stelzer, B., Marino, A., Micela, G., López-Santiago, J., & Liefke, C. 2014, MNRAS, 442, 343
Tal-Or, L., Trifonov, T., Zucker, S., Mazeh, T., & Zechmeister, M. 2019, MNRAS, 484, L8
Teegarden, B. J., Pravdo, S. H., Hicks, M., et al. 2003, ApJ, 589, L51
Trifonov, T., Kürster, M., Zechmeister, M., et al. 2018, A&A, 609, A117
Weinberger, A. J., Boss, A. P., Keiser, S. A., et al. 2016, AJ, 152, 24
Wells, R., Poppenhaeger, K., Watson, C. A., & Heller, R. 2018, MNRAS, 473, 345
Wenger, M., Ochsenbein, F., Egret, D., et al. 2000, A&AS, 143, 9
West, A. A., Hawley, S. L., Bochanski, J. J., et al. 2008, AJ, 135, 785

West, A. A., Weisenburger, K. L., Irwin, J., et al. 2015, ApJ, 812, 3
Wildi, F., Blind, N., Reshetov, V., et al. 2017, Proc. SPIE, 10400, 1040018
Wright, N. J., Drake, J. J., Mamajek, E. E., & Henry, G. W. 2011, ApJ, 743, 48
Zechmeister, M., & Kürster, M. 2009, A&A, 496, 577
Zechmeister, M., Anglada-Escudé, G., & Reiners, A. 2014, A&A, 561, A59
Zechmeister, M., Reiners, A., Amado, P. J., et al. 2018, A&A, 609, A12
Zeng, L., Sasselov, D. D., & Jacobsen, S. B. 2016, ApJ, 819, 127

[1] Institut für Astrophysik, Georg-August-Universität, Friedrich-Hund-Platz 1, 37077 Göttingen, Germany
e-mail: zechmeister@astro.physik.uni-goettingen.de
[2] Institut de Ciències de l'Espai (ICE, CSIC), Campus UAB, C/Can Magrans s/n, 08193 Bellaterra, Spain
[3] Institut d'Estudis Espacials de Catalunya (IEEC), 08034 Barcelona, Spain
[4] Centro de Astrobiología (CSIC-INTA), ESAC campus, Camino bajo del castillo s/n, 28692 Villanueva de la Cañada, Madrid, Spain
[5] Instituto de Astrofísica de Andalucía (IAA-CSIC), Glorieta de la Astronomía s/n, 18008 Granada, Spain
[6] Instituto de Astrofísica de Canarias (IAC), Vía Láctea s/n, 38205 La Laguna, Tenerife, Spain
[7] Departamento de Astrofísica, Universidad de La Laguna (ULL), 38206 La Laguna, Tenerife, Spain
[8] Department of Geophysics, Raymond and Beverly Sackler Faculty of Exact Sciences, Tel Aviv University, Tel Aviv 6997801, Israel
[9] School of Physics and Astronomy, Queen Mary, University of London, 327 Mile End Road, London, E1 4NS, UK
[10] Landessternwarte, Zentrum für Astronomie der Universität Heidelberg, Königstuhl 12, 69117 Heidelberg, Germany
[11] Centro Astronómico Hispano-Alemán (CSIC-MPG), Observatorio Astronómico de Calar Alto, Sierra de los Filabres-04550 Gérgal, Almería, Spain
[12] Leiden Observatory, Leiden University, Postbus 9513, 2300 RA, Leiden, The Netherlands
[13] Max-Planck-Institut für Sonnensystemforschung, Justus-von-Liebig-Weg 3, 37077 Göttingen, Germany
[14] Departamento de Astronomía, Universidad de Chile, Camino El Observatorio 1515, Las Condes, Santiago, Chile
[15] Instituto Nacional de Astrofísica, Óptica y Electrónica, Luis Enrique Erro 1, Sta. Ma. Tonantzintla, Puebla, Mexico
[16] Departamento de Física de la Tierra y Astrofísica & IPARCOS-UCM (Instituto de Física de Partículas y del Cosmos de la UCM), Facultad de Ciencias Físicas, Universidad Complutense de Madrid, 28040 Madrid, Spain
[17] Max-Planck-Institut für Astronomie, Königstuhl 17, 69117 Heidelberg, Germany
[18] Thüringer Landessternwarte Tautenburg, Sternwarte 5, 07778 Tautenburg, Germany
[19] Hamburger Sternwarte, Universität Hamburg, Gojenbergsweg 112, 21029 Hamburg, Germany
[20] Department of Exploitation and Exploration of Mines, University of Oviedo, Oviedo, Spain
[21] Department of Earth and Planetary Science, The University of Tokyo, 7-3-1 Hongo, Bunkyo-ku, Tokyo 113-0033, Japan
[22] Observatorio Astronómico Nacional (OAN-IGN), Apartado 112, 28803 Alcalá de Henares, Spain
[23] FRACTAL SLNE. C/ Tulipán 2, P13-1A, 28231 Las Rozas de Madrid, Spain
[24] Centro de Astrobiología (CSIC-INTA), Carretera de Ajalvir km 4, 28850 Torrejón de Ardoz, Madrid, Spain
[25] Institut für Theoretische Physik und Astrophysik, Leibnizstraße 15, 24118 Kiel, Germany
[26] Institut für Astronomie und Astrophysik, Eberhard Karls Universität, Sand 1, 72076 Tübingen, Germany
[27] Department of Signal Theory and Communications, Universidad Carlos III de Madrid, Av. de la Universidad 30, 28911 Leganés, Spain
[28] Gregorio Marañón Health Research Institute, Doctor Esquerdo 46, 28007 Madrid, Spain
[29] Department of Physics, University of Rome Tor Vergata, Via della Ricerca Scientifica 1, 00133 Rome, Italy
[30] INAF – Osservatorio Astrofisico di Torino, Via Osservatorio 20, 10025 Pino Torinese, Italy
[31] International Institute for Advanced Scientific Studies (IIASS), Via G. Pellegrino 19, 84019 Vietri sul Mare (SA), Italy
[32] IES Montes Orientales, Departamento de Matemáticas, Carretera de la Sierra 31, 18550 Iznalloz, Granada, Spain
[33] Department of Astronomy, The University of Tokyo, 7-3-1 Hongo, Bunkyo-ku, Tokyo 113-0033, Japan
[34] Astrobiology Center, 2-21-1 Osawa, Mitaka, Tokyo 181-8588, Japan
[35] JST, PRESTO, 7-3-1 Hongo, Bunkyo-ku, Tokyo 113-0033, Japan
[36] National Astronomical Observatory of Japan, 2-21-1 Osawa, Mitaka, Tokyo 181-8588, Japan
[37] Weizmann Institute of Science, 234 Herzl Street, Rehovot 761001, Israel
[38] School of Physics, University College Dublin, Belfield, Dublin 4, Ireland
[39] European Southern Observatory, Alonso de Córdova 3107, Vitacura, Casilla 19001, Santiago de Chile, Chile
[40] Diseño Sistemas Ópticos, Maria Moliner 9B, 41008 Sevilla, Spain
[41] The Department of Astronomy and Astrophysics, University of Chicago, 5640 S. Ellis Ave, Chicago, IL 60637, USA
[42] Universidad de Granada, Av. del Hospicio, s/n, 18010 Granada, Spain
[43] Optical System Engineering, Kirchenstr. 6, 74937 Spechbach, Germany

Appendix A: Photometric facilities

Table A.1. Photometric facilities.

Acronym	Location	Tel. (m)	FOV (arcmin^2)	CCD	Scale (arcsec pix^{-1})	Band(s)
CAHA 1.23	Calar Alto Observatory	1.23	17.9×17.9	$2k \times 2k$	0.50	I
LCO	Las Cumbres Observatory Global Telescope	0.40	29.2×19.5	$3k \times 2k$	0.57	i'
MEarth	Fred Lawrence Whipple Observatory	0.40	26.0×26.0	$2k \times 2k$	0.76	RG715, I
MONET-S	South African Astronomical Observatory	1.20	12.6×12.6	$2k \times 2k$	0.37	R
MuSCAT2	TCS Teide Observatory	1.52	7.4×7.4	$1k \times 1k$	0.44	$griz_s$
SNO T150	T150 Sierra Nevada Observatory	1.50	7.9×7.9	$2k \times 2k$	0.23	VRI
SNO T90	T90 Sierra Nevada Observatory	0.90	13.2×13.2	$2k \times 2k$	0.38	R
TJO	TJO Montsec Astronomical Observatory	0.80	12.3×12.3	$2k \times 2k$	0.36	R

CAHA 1.23. The Centro Astronómico Hispano-Alemán operates the 1.23 m telescope for photometric monitoring projects. The CCD imager mounted at the Cassegrain focus covers a squared field of view (FOV) of 17.9 arcmin and is equipped with a 2k×2k SITE CCD. Observations were made in the I band.

LCO. We obtained i'-band images using the 40 cm telescopes of the Las Cumbres Observatory (LCO) network. The telescopes are equipped with a $3k \times 2k$ SBIG CCD camera with a pixel scale of 0.571 arcsec, providing a field of view of 29.2×19.5 arcmin^2. The data were processed using the `Banzai` pipeline (McCully et al. 2018). The photometry of the 2017 set was extracted with `IRAF-PHOT` and the 2018 set with `AstroImageJ` (Collins et al. 2017).

MEarth. Since 2008, the MEarth project (Berta et al. 2012) monitors more than 2000 M dwarfs with eight robotic 40 cm telescopes (f/9 Ritchey-Chrétien Cassegrain) at the Fred Lawrence Whipple Observatory (Arizona, USA). Each telescope covers a squared 26 arcmin field of view with a 2048×2048 CCD (0.76 arcsec pix^{-1}). MEarth generally used an RG715 long-pass filter, except for the 2010–2011 season, when a $I_{715-895}$ interference filter was chosen. Additionally, Teegarden's Star was monitored with a second telecope (#8) in 2013 and 2014. We made use of the archival data from the seventh MEarth data release, DR7[11], which provides long-term monitoring of Teegarden's Star over about 10 yr.

MONET-S. The 1.2 m MONET/South telescope (MOnitoring NEtwork of Telescopes) is located at the South African Astronomical Observatory (Northern Cape, South Africa). It is equipped with a Finger Lakes ProLine $2k \times 2k$ e2v CCD and has a 12.6×12.6 arcmin^2 field of view. We performed aperture photometry with `AstroImageJ` using eight comparison stars.

MuSCAT2. The Multicolor Simultaneous Camera for studying Atmospheres of Transiting exoplanets 2 (MuSCAT2; Narita et al. 2019) is mounted at Telescopio Carlos Sánchez in Teide observatory (Tenerife, Spain). MuSCAT2 observes simultaneously in the g, r, i, and z_s bands using a set of dichroics to split the light between four separate cameras with a field of view of 7.4×7.4 arcmin^2 (0.44 arcsec pix^{-1}). MuSCAT2 is designed to be especially efficient for science related to transiting exoplanets and objects varying on short timescales around cool stellar types. Aperture photometry is calculated using a Python-based pipeline especially developed for MuSCAT2 (see Narita et al. 2019, for details).

Table A.2. Properties of the photometric data sets [(a)].

Data set	Season	ΔT (d)	N_{obs}	rms (mag)
CAHA 1.23	2018	0.3	124	0.003
LCO 17	2017	421	116	0.012
LCO 18	2018	431	148	0.014
ME T1 08-1	2008–2009	351	145	0.007
ME T1 08-2	2009–2010	377	342	0.007
ME T1 11	2010–2011	260	504	0.007
ME T1 14-1	2011–2015	1473	824	0.004
ME T1 14-2	2011–2015	1454	638	0.004
ME T8 14-1	2013–2014	139	728	0.004
ME T8 14-2	2013–2014	87	429	0.004
ME all	2008–2015	2577	2547	0.004
MONET-S	2018	22	1201	0.004
MuSCAT2 g	2018	18	563	0.006
MuSCAT2 r	2018	55	918	0.004
MuSCAT2 i	2018	50	827	0.001
MuSCAT2 z	2018	28	360	0.002
SNO V	2017–2019	540	2205	0.006
SNO R	2017–2019	540	2340	0.005
SNO I	2017–2019	540	2231	0.008
SNO-T90 R	2018	1	236	0.003
SNO-T150 R	2018	20	1274	0.002
TJO 17	2017	54	2280	0.011
TJO 18	2018	35	475	0.002

Notes. [(a)]Data set identifier, season, time span, number of observations, and rms in relative flux after removing the strongest signal in each set.

SNO. The T150 telescope at Sierra Nevada Observatory (Granada, Spain) is a 1.5 m Ritchey-Chrétien telescope equipped with a CCD camera VersArray $2k \times 2k$, FOV 7.9×7.9 arcmin^2 (Rodríguez et al. 2010). Two sets of observations were collected in Johnson V, R, and I filters: one set consisted of 54 epochs obtained during the period July 2017 to January 2018, while the other set consisted of 53 epochs collected between July 2018 and January 2019. Each epoch typically consisted of 20 observations per night in each filter of 100, 50, and 20 s. In addition, the T150 was also used for transit search (SNO T150-R in Table A.2) during two nights in the R filter. The T90 telescope at SNO (SNO T90-R in Table A.2) and R filter were also used for transit search during one night.

TJO. The Telescopi Joan Oró is an 80 cm telescope located in the Montsec Astronomical Observatory (Lleida, Spain). Photometry in Johnson *R* filter was obtained with the MEIA2 instrument, a 2k×2k Andor CCD camera, with a pixel scale of 0.36 arcsec and a squared field of view of 12.3 arcmin. The images were processed with the ICAT pipeline (Colome & Ribas 2006) and `AstroImageJ`.

Appendix B: GLS periodograms for activity indicators

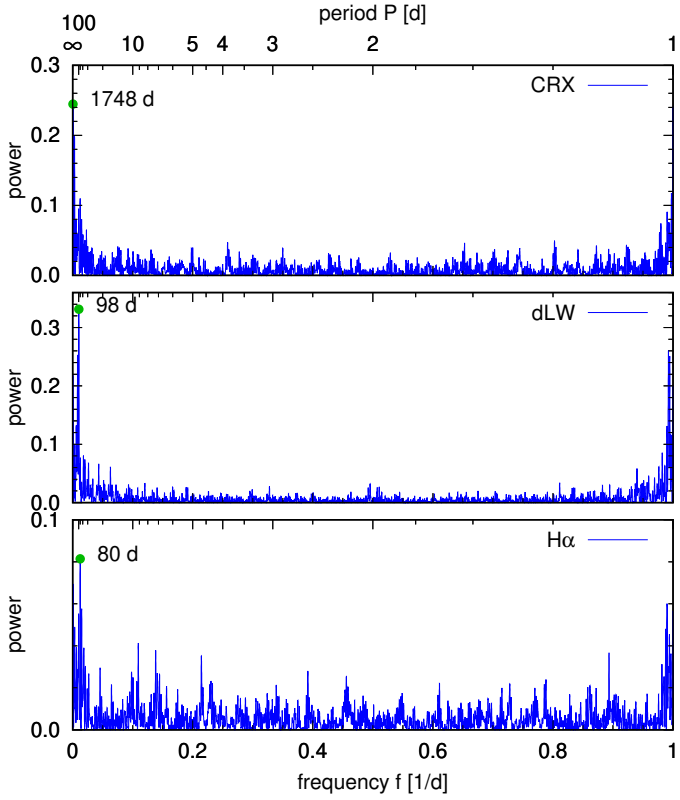

Fig. B.1. GLS periodograms for CRX, dLW, and Hα index.

Appendix C: MCMC corner plots

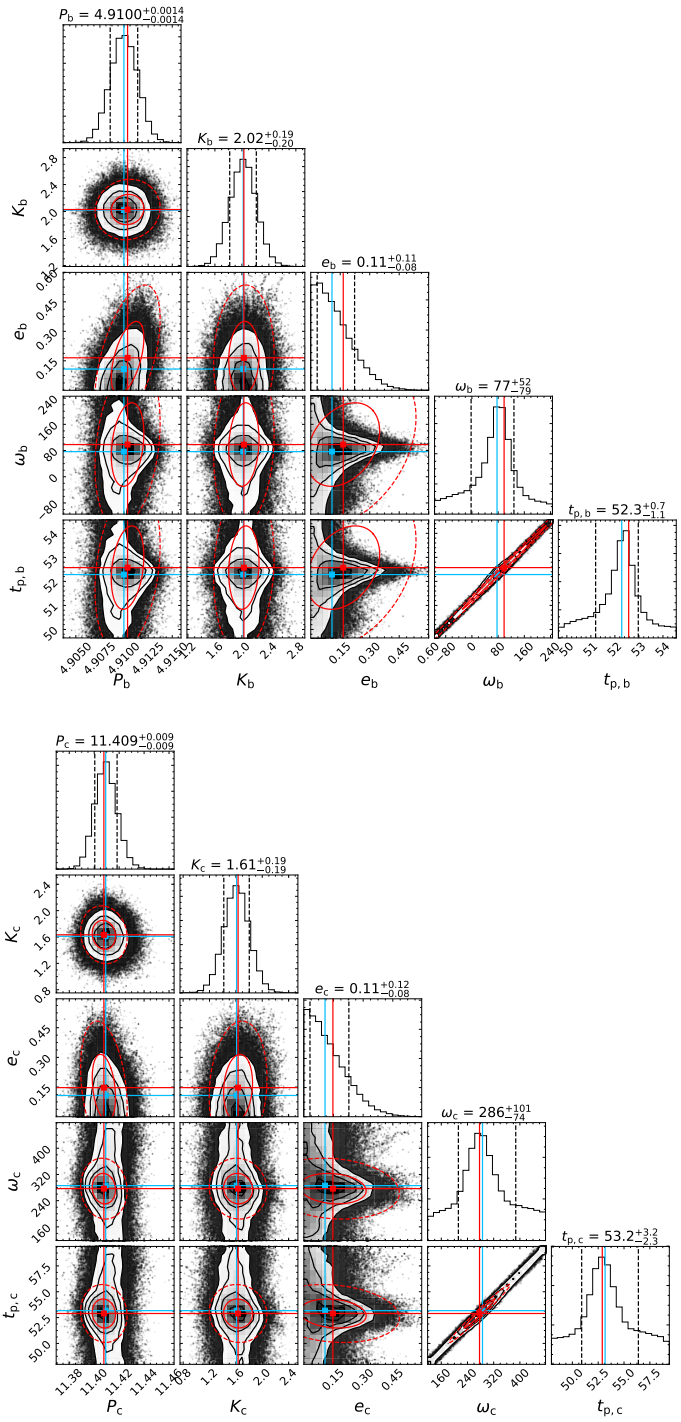

Fig. C.1. MCMC posterior distribution for Keplerian parameters of planets b (*top*) and c (*bottom*). The median values and 15.87 and 84.13 % are indicated in light blue and black dashed lines, while best-fit values and 1σ and 2σ levels from covariance matrix are overplotted in red.

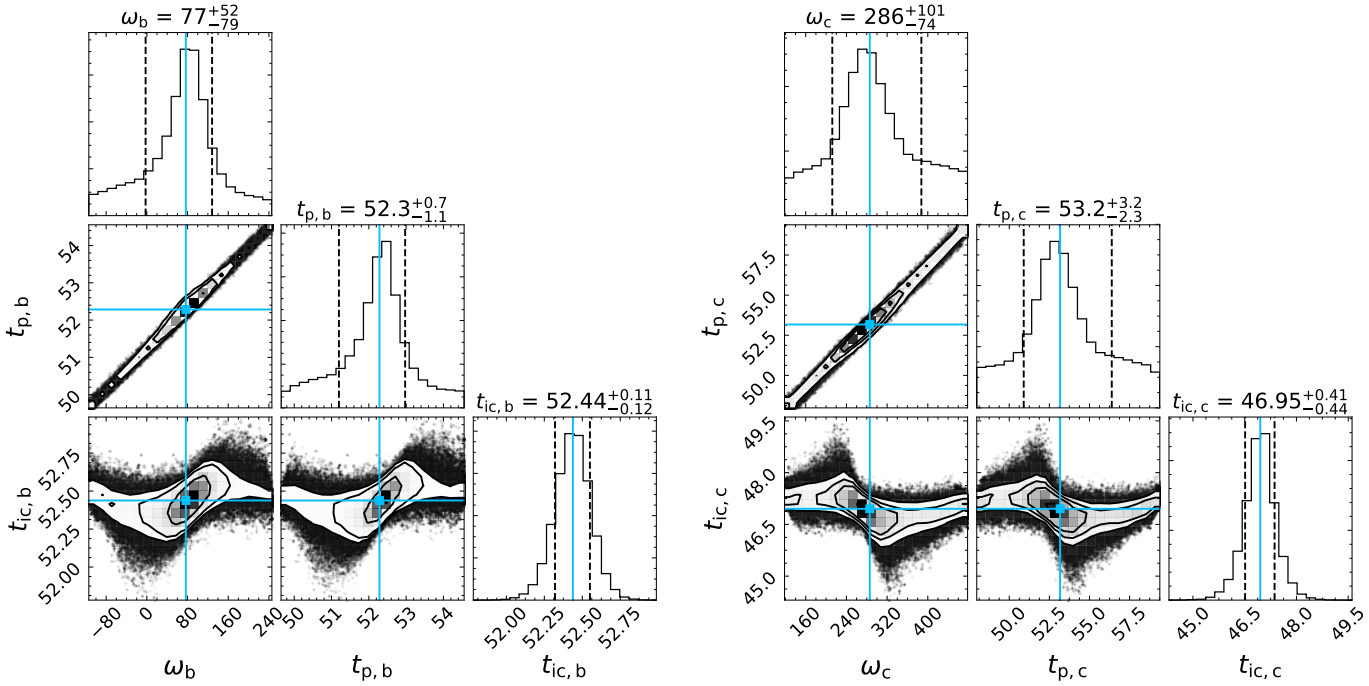

Fig. C.2. MCMC posterior distribution for inferior conjunction times of planets b (*left*) and c (*right*).

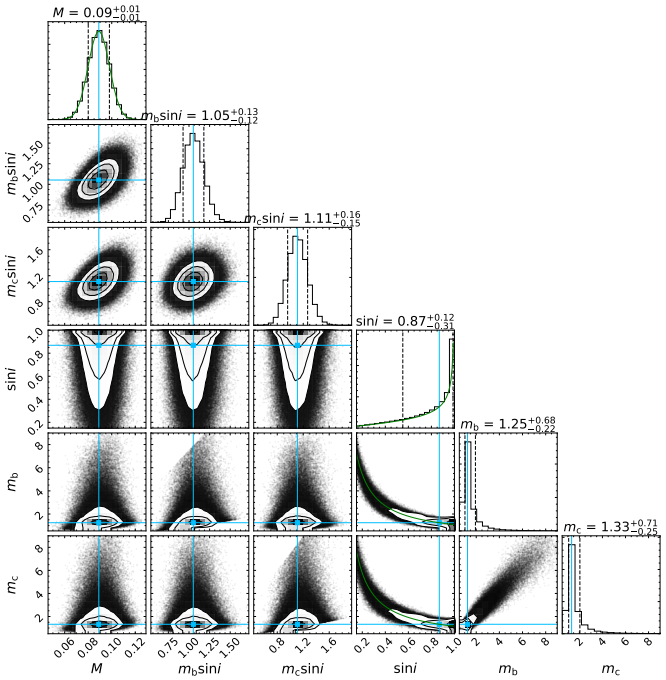

Fig. C.3. MCMC posterior distribution for derived masses of planets b and c. The priors for stellar mass M and inclination $\sin i$ are overplotted in green.